The manuscript is a preprint uploaded to EarthArxiv. This preprint has been submitted for publication to *Scientific Reports* on the 03th of March 2021.

Authors encourage downloading the latest manuscript version from EarthArXiv, and welcome comments, feedback and discussions anytime.

Please, feel free to get in contact: utsav@iiserpune.ac.in

Title: Thrusts control the thermal maturity of accreted sediments

Authors: Utsav Mannu[1,*], David Fernández-Blanco[2], Ayumu Miyakawa[3], Taras Gerya[4], and Masataka Kinoshita[5]

Affiliations:

[1]Department of Earth and Climate Science, Indian Institute of Science Education and Research, Pune, India

*corresponding author: utsav@iiserpune.ac.in

[2] Barcelona Center of Subsurface Imaging, Institut de Ciències del Mar (ICM-CSIC), Barcelona, Spain;

[3]Geological Survey of Japan, AIST

[4]Institute of Geophysics, ETH Zurich

[5]Earthquake Research Institute, UTokyo

Thrusts control the thermal maturity of accreted sediments

Utsav Mannu[1,*], David Fernández-Blanco[2], Ayumu Miyakawa[3], Taras Gerya[4], and Masataka Kinoshita[5]

[1]Discipline of Earth Sciences, Indian Institute of Technology, Gandhinagar, India

*corresponding author: utsav.mannu@iitgn.ac.in

[2] Barcelona Center of Subsurface Imaging, Institut de Ciències del Mar (ICM-CSIC), Barcelona, Spain;

[3]Geological Survey of Japan, AIST

[4]Institute of Geophysics, ETH Zurich

[5]Earthquake Research Institute, UTokyo

13

14 # ABSTRACT

15

16 Thermal maturity assessments of hydrocarbon-generation potential and thermal history rarely consider how
17 upper-plate structures developing during subduction influence the trajectories of accreted sediments. Our
18 thermomechanical models of subduction support that thrusts evolving under variable sedimentation rates
19 and décollement strengths fundamentally influence the trajectory, temperature, and thermal maturity of
20 accreting sediments. This is notably true for the frontal thrust, which pervasively partitions sediments along
21 a low and a high maturity path. Our findings imply that interpretations of the distribution of thermal maturity
22 cannot be detached from accounts of the length and frequency of thrusts and their controlling factors.
23 Taking these factors into consideration, our approach reduces former inconsistencies between predicted and
24 factual thermal maturity distributions in accretionary wedges and provides a first-order predictive indicator
25 for thermal maturity distribution based on known fault architectures.

26

27

28

29

30

1. Introduction

Organic material transforms into coal, oil, and gas at rates primarily controlled by temperature[1]. This transformation, critical for the hydrocarbon industry, is also useful to study the tectonic and sedimentary evolution of basins and orogens[2–4]. The extent of this transformation in sediments, known as thermal maturity, can be measured as vitrinite reflectance; the percentage of incident light reflected from the surface of vitrinite particles in those sediments[5]. Thermal maturity has been used to estimate the thermal evolution of igneous intrusions[6] and seismic slip[7], the extent of diagenesis and low-grade metamorphism[8,9], porosity and compaction in basin sediments[10], as well as the geothermal history of accreting material during subduction[11–13].

Inferences on the geothermal history of subduction margins based on thermal maturity depend on the trajectory followed by the accreting sediments[14]. Low-temperature high-pressure metamorphic rocks in the subduction wedge are often attributed to the pressure maxima that typically predates the temperature maxima in sediments accreted in the wedge[15]. However, numerical models[16] and field observations[17] have indicated the existence of complicated patterns in sediment trajectories. As the orogenic wedge evolves, sediments accreting along different paths reach different depths and velocities and are exposed to different regional peak temperatures. Miyakawa (2019)[14] proposed to subdivide these trajectories based on their final characteristics such as thermal maturity. As a result, the spatiotemporal evolution of the sediments which regulates thermal maturity is controlled, to a first-order, by the partition of incoming sediments along two end-member pathways; (i) a deeper path leading to elevated thermal maturities, the ***high thermal-maturity path***, and (ii) a shallower path resulting in low thermal maturity, the ***low thermal-maturity path***[14].

Although a number of researchers have studied the diversity particle paths by their P-T evolution in accreted and underthrusted sediments, in presence of surface processes, distribution of surface processes, in both analytical and numerical models[18–22], its correlation or lack thereof with its pre-accreted state has not been suitably investigated. Much remains to be explored regarding how the partition of high/low

55 thermal maturity paths and the general translation of sediments occurs inside the wedge, given the
56 conventional assumption that accreting sediments remain at the same relative depth[21] and translate along
57 the adjacent "layers" without vertical mixing throughout the tectonic evolution of the wedge[23,24] to yield
58 this diversity of sediment paths. To better understand the time-depth paths of wedge sediments, their
59 dependence on the initial state of undeformed sediments, and thus their thermal maturity, the factors that
60 control the evolution of subduction-accretion systems, like sedimentation, erosion, and décollement
61 strength[25,26], ought to be considered.

62 Here, we explore in detail the impact that a realistic account of accretion in a subduction wedge has
63 on the thermal maturity of its sediments. We simulate subduction-accretion using 2D finite-difference
64 thermomechanical models that incorporate empirical thermal conductivity values from the Nankai
65 accretionary margin. We track the evolution of thermal maturity by computing vitrinite reflectance on
66 markers in the model mesh as the wedge develops by accretion under different sedimentation rates and
67 décollement strengths. These factors notably alter the trajectories and thermal maturities of incoming
68 sediments. Particularly, thrusts define sharp thermal maturity boundaries leading to stark differences in the
69 thermal maturity of sediments that accrete in different thrust blocks, even when they follow similar
70 trajectories and lay nearby.

71 2. Methods

72 We employ I2VIS, a conservative[27] finite-difference 2-D thermomechanical subduction-accretion model
73 with visco-plastic/brittle rheology.[28] The code solves the governing equations for conservation of mass,
74 momentum, and heat as well as the advection equation with a non-diffusive marker-in-cell scheme[27]
75 constrained by thermal conductivity values inferred from Nankai accretionary wedge[29]. Our numerical
76 approach has several advantages over earlier modelling attempts to simulate thermal maturity in an
77 accretionary wedge[14] , such as a more realistic geothermal profile, thermal evolution, and dynamic sediment
78 subduction. The supplementary material contains additional information regarding the governing equations,

the modified thermal conductivity formulations based on the C0002 borehole in the Nankai accretionary wedge, boundary conditions, rheological model, and surface processes.

2.1 An improved thermal maturity calculation

Given that assessments of thermal maturity are inherently reliant on the distribution of temperature inside the wedge, any attempt to model thermal maturity needs a realistic temperature gradient in the wedge. We incorporate this by modifying the thermal conductivity computation for sediments and décollement (see Table 1 and section 1 in the provided supplementary text) to match the empirical relationship between depth and thermal conductivity, as measured on core samples in the borehole IODP Site C0002[29,32]. Both for the same accretionary wedge is scarce to find, and to our knowledge, the C0002 borehole in Nankai accretionary wedge along the Kumano forearc basin is the only place with available datasets for both thermal conductivity and thermal maturity values[33]. The model computes the Vitrinite Reflectance (Ro%) of each marker to estimate the thermal maturity of sediments during the model run. Ro% is set to 0.2 in sediment markers at the start of the model, while Ro% in markers for other rocks, air, and water is undefined. Thereafter, the model computes Ro% on each marker as a function of temperature (T), time (t), and amount of fixed carbon as a percentage, f_c[34]:

$$Ro = exp(lnRo_{init} + 3.7f_c) \qquad \textbf{(eq. 1)}$$

$$f_c = 0.85\left(1 - exp\left(-Aexp\left(\frac{-E\Delta t}{RT}\right)\right)\right) \qquad \textbf{(eq. 2)}$$

$$E = 40.7lnRo + 227 \qquad \textbf{(eq. 3)}$$

Where Ro is the vitrinite reflectance, f_c is the amount of fixed carbon in percentage, Ro_{init} is the initial vitrinite reflectance (0.2), A is a frequency factor (1.0×10^{13}/s), R is the gas constant, Δt is the duration of the calculation interval, and E is the activation energy.

2.2 Experimental Strategy

Here, we present a total of 9 models that vary in their effective basal friction or their effective sedimentation rate to discern patterns of thermal maturity evolution in wedge sediments. We nominate models with variable effective internal angles with capital letters and models with variable sedimentation rates with numeric subindices. Models $\mathbf{W_0}, \mathbf{M_0}, \mathbf{S_0}$ have no sedimentation and effective internal angle values for the décollement of ϕ_b= 2°, 7°, and 12°, which we conceptualize loosely as weak (W), medium (M), and strong (S) décollements. The chosen range of effective decollement strength is well within the range of values postulated by several studies for the Nankai accretionary wedge[35].

The rest of the models shown here, $\mathbf{M_{0.1}}$-$\mathbf{M_{0.6}}$, have a medium-strength décollement and variable effective sedimentation rate ranging from 0.1 to 0.6 mm/yr. Sedimentation occurs at the trench in all of the models presented in this study from sea to land. With these models, we evaluate the particle trajectory and Ro% of accreting sediments as a function of décollement strength ($\mathbf{W_0}, \mathbf{M_0}, \mathbf{S_0}$) and sedimentation rate ($\mathbf{M_{0.1}}$-$\mathbf{M_{0.6}}$). To restrict the number of parameters influencing our observations, models have no erosion. . Moreover, all models lack surface processes during the first ~2.5 Myr and have sedimentation thereafter. Sediments used in the model have an angle of friction of 30° and a strain-softened value of 15° after a threshold of 0.5-1.5 strain. The coefficient of friction increases linearly between the thresholds. Sedimentation rates are the effective sedimentation rate computed after the model run and are thus not prescribed a priori. This choice ensures that the range of average sedimentation in all our models (0-0.6 mm/yr) lies within observed sedimentation rates in our chosen natural equivalent, the Nankai accretionary wedge in the south-western subduction margin of Japan[36]. Table 2 provides more details about the model run and prescribed sedimentary conditions.

3. Results

Subduction begins at 0.1 Myr as the weak material between continental and oceanic plates fails (see supporting information movies). Continued and sustained accretion of sediments against the deforming

continental crust forms the accretionary wedge from the interplate contact landwards. After ~5 Myr, all models develop a distinct wedge in agreement with the critical taper theory[37]. Taper angles increase by more than an order of magnitude as effective internal angles increase by ~10° (Table 2). Concretely, whereas models with a relatively weaker décollement, as W_0 (ϕ_b= 2°), have taper slopes of 1.2°± 0.4°, models with very strong décollement, as S_0 (ϕ_b= 12°), have slopes as steep as 18.8 ± 3.1°. Contrarily, increasing trench sedimentation rate leads to lower wedge-taper angles, albeit with a larger standard deviation (Table 2). Steeper surface slopes with increased décollement strengths and gentler slopes with increased sedimentation are well-known effects that have been confirmed by previous numerical[25,38] and analytical[39,40] models.

Models without trench sedimentation grow solely by accretion of incoming seafloor sediments, with frequent nucleation of frontal thrusts. Models with weaker décollements develop thrusts that are the lengthier and remain active for shorter periods. This is clear when comparing, for models with increasingly strong decollements (W_0, M_0, S_0), the average distance between first and second frontal thrust and their average time of nucleation; these are 4.0 ± 2.2 km, 3.8 ± 1.6 km, and 3.4 ± 2.2 km, and 0.20 Myr, 0.25 Myr and 0.34 Myr, respectively. Increasing sedimentation rate also leads to an increase in thrust sheet length. Compared to the model without sedimentation, models with higher sedimentation rates have lengthier thrust sheets that remain active for longer periods (Table 2). All décollement-strength models without sedimentation (W_0, M_0, and S_0) exhibit a temperature gradient that corresponds well with the temperature profile observed in the boreholes at IODP Site C0002 in the Kumano forearc basin, on top of the Nankai accretionary wedge (Fig. S2).

3.1 Thermal maturity of the wedge

Sediments are more thermally mature in wedges that have a higher sedimentation rate or décollement strength. For example, the mean R_0% of simulations for wedges with high sedimentation ($M_{0.6}$) is 0.21

(43%) higher than in those without sedimentation (M_0) (Table 2, Fig 1). Similarly, simulations of wedges with the strongest décollement have the highest mean R_0% of all the simulations presented in this study.

Thermal maturity values increase with depth and landward distance from the trench to the forearc high (Fig. 1). As a result, sediments at the core of the wedge consistently reach the highest maturity. The absolute value of R_0% and the rate at which thermal maturity values increase landward from the trench are large for wedges with high sedimentation rate or high décollement strength. Comparing the values of R_0% (Fig. 1E) along an arbitrary horizon in several models (Fig. 1A-1D) emphasizes this result; the model with the highest sedimentation attains the maximum R_0% of 1.45, whereas the rate of landward increase in thermal conductivity is highest for the wedge with the strongest décollement (Fig. 1). All models show a decrease in thermal maturity landward of the forearc high, commonly of 0.2 R_0%. Other interesting observations that we explore below are the increased thermal maturity occurring in the vicinity of thrusts (Fig. 1C) and the reversal in sediment maturity around out-of-sequence thrust active over longer times (Fig. 1B, 1D).

3.2 Sediment trajectory inside the wedge

Sediments follow high-maturity paths in larger proportions in wedges with a higher décollement strength or sedimentation rate. We demonstrate this effect by computing the average depth of the trajectories normalized by the thickness of the wedge in a parameter Y_n that ranges from 0 to 1 and has a smaller value the closer the trajectory of sediments is to the décollement (Fig. 2). Models with weak and medium strength décollements (W_0 and M_0 in Fig. 2) have $Y_n < 0.5$ for slightly above half of the trajectories of its sediments (58% and 52% respectively), indicating depths closer to the décollement. Models with high strength décollement or sedimentation rates (S_0 and $M_{0.6}$ in Fig. 2) have four-fifths and two-thirds of all sediments (79% and 64% respectively) following depth paths closer to the décollement than to the surface. These models also include large contiguous zones, such as B_{S0}-D_{S0} and $D_{M0.6}$-$F_{M0.6}$, where all sediment trajectories have $Y_n < 0.25$ (Fig 2). Since the depth of the sedimentary trajectories correlates with log(R_0%), sediments

in wedges with lower Y_n values have high thermal maturity (Fig 3). Furthermore, Fig.3 shows that models with higher sedimentation rate and décollement strength tend to have higher R_0% at similar Y_n.

3.3 Patterns of trajectory and thermal maturity in incoming sediments

We create a contour map of the thermal maturity of sediments at 7.5 Myr of the model run, mapped to their spatial position 5 Myr earlier (at 2.5 My of model run) (Fig. 4) to analyse the spatial correlation between sediment position (depth and distance) from the trench and thermal maturity. We define a thermal maturity boundary where R_0% = 1.5 (line $P_{1.5}$ in Fig 4) and differentiate sediments below and above it, which have a relatively higher and lower maturity (R_0% > 1.5 and R_0% < 1.5 respectively).

Our defined thermal maturity boundary has sharp changes with distance from the trench that relate to changes in sediment trajectory (Fig. 4). The thermal maturity boundary is variable along the horizontal length of the wedge and has a periodicity increasing in distance with higher décollement strength and sedimentation rate (Fig. 4; Table 2). Whereas the thermal maturity boundary has a periodicity at horizontal distances of ~16 km and 22 km in weak- and medium-strength décollement models (W_0 and M_0), the periodicity decreases to one third, to ~50 km and 57 km, when décollement strength or sedimentation rate are high (S_0 and $M_{0.6}$), respectively. The increase in periodicity due to sedimentation can also be observed in models M_0-$M_{0.6}$ presented in Table 2.

Increasing sedimentation rates or décollement strength leads sediments at shallow positions onto high-maturity routes closer to décollement (Fig. 4). Whereas in wedges with weak decollements (W_0), only 1% of the shallowest 250m of incoming sediments reach R_0% > 0.5, more than one-third (37%) of sediments reach this value in wedges with strong décollements (S_0). The effects of décollement strength in the thermal maturity of sediments can be quantified as well at deeper levels, with one-fifth and two-thirds of sediments surpassing values of R_0% = 1.5 at 750 m depth (21% and 71% respectively) in weak and strong-decollement wedges, respectively. Increasing the sedimentation rate has similar effects. In wedges from models without

sedimentation, only 4% of the top 250 m of sediments yield Ro% > 1.5, while up to 40% of them surpass the thermal maturity boundary in the models with a sedimentation rate of 0.6 mm/yr ($M_{0.6}$). In sum, the proportion of sediments in the top 250 m and 750 m of the wedge that reach $R_0\%$ > 1.5 steadily increases with both sedimentation rate and décollement strength (Table 2).

4. Discussion

Our models achieve realistic thermal maturity distributions thanks to unique computational advantages over models in the previous studies[14,25,41], despite several relevant assumptions. Models are simplified by assuming no elasticity, predefined décollement, no erosion, and using simple and uniform rheology, and either have an insufficient resolution or lack empirical relations to simulate the compaction of sediments and processes of multiscale fluid flow. Although these assumptions hinder a wholesale comparison between our simulations and natural examples of accretionary wedges, we are confident of the thermal maturity patterns of our models. Our estimated $R_0\%$ values for model S_0 are in very good agreement with the $R_0\%$ values measured for the borehole C0002 Nankai accretionary wedge (used for thermal conductivity values) by Fukuchi et. al. 2009 (Figure 5). Additionally, models W_0 and M_0 show similar trends, albeit at a much greater depth of 3.2 km and 7.4 km respectively. Furthermore, our models also correlate with the patterns of P-wave velocity[42] (Fig S4). This correlation between the patterns of thermal maturity and P-wave velocity has been shown for Nankai[43,44] and Hikurangi[45] margins. Models compute realistic thermal maturity distributions thanks to several key improvements. Firstly, our models calculate temperature gradients that evolve at long time intervals and thus closely replicate accretionary wedges in nature (Fig. S2). This enables the simulation of realistic temperature profiles based on thermal conductivity values derived empirically from natural accretionary wedges, as in our case, the Nankai margin[29] Secondly, our simulations account for the effects that thermal and isostatic feedback from the oceanic lithosphere have on the evolution of the wedge by simulating plate subduction at a large scale rather than just the accretionary wedge[14]. Finally, our method calculates the vitrinite reflectance of sediments on each marker of the mesh.

219 This relevantly expands the numerical precision of previous efforts[25,41], as it allows tracking the evolution
220 of thermal maturity in sediments more efficiently. This capacity to accurately estimate thermal maturity in
221 each marker informs the research questions of this study and allows inferences beyond those of depth-
222 dependent thermal maturity distributions.

223 The thermal maturity of the wedge increases landward, as signalled by the landward increase in
224 R_0% (Fig. 1). This has been observed in natural accretionary wedges[13] and other numerical models of
225 accretion[14], resulting from the long-term deformation of older accreted sediments and the backstop-forced
226 exhumation in the wedge. Our models show that the rate of landward rise in thermal maturity is faster for
227 thicker wedges (Fig 1). This is the case for wedges with high basal strength and larger sedimentation input,
228 for sediments in thicker wedges deform more prominently than those in their thinner counterparts.
229 Simulations also show that sediments reach deeper levels in thicker wedges and that this increases the
230 overall thermal maturity of the wedge. Also, increased exhumation rates and steeper thermal maturity
231 gradients occur in the wedge interior, as the continental backstop deflects sediment trajectories upwards
232 during accretion (Fig. 2). As a result, for the geometry of the backstop used in our models, backstop-forced
233 exhumed material is, on average, thermally more mature.

234 Our models expose two relevant cases where the increase of thermal maturity with depth or
235 landward is relevantly altered: on-fault increase and fault-block inversion. Our models attest to the steep
236 rise in thermal maturity of sediments at fault sites (Fig. 1C). This is well documented in nature, as for
237 boreholes C0004 and C0007[11]. However, on-fault increases in thermal maturity are comparatively smaller
238 in our simulations and lack the marked increase in Ro% observed at fault sites in nature. This is primarily
239 due to our models developing wider fault zones than their natural equivalents and the subsequent
240 acceleration in the thermal diffusion occurring in simulated thrusts. During fault-block inversions, the
241 positive gradient of thermal maturity with depth is inverted by thrusting relatively mature sediments over
242 less mature sediments[12], as shown in Fig. 3B. This is known from natural observations, as along the Fukase

Fault in Shimanto accretionary wedge[46] and underneath the forearc basin in Nankai accretionary wedge[33], and previous modelling efforts[14].

Collation of the above implies that the thermal maturity of accretionary wedges results from the general increase of thermal maturity (i) with depth and (ii) landward, as well as from its (iii) modification by thrust faults. Our models suggest thermal maturity inversions by thrusting, which are commonplace in accretionary contexts, are the primary cause of thermal maturity differentiation among wedges with initially similar geothermal gradients. In other words, the strong differentiation in the trajectory of sediments led by thrusting has a larger influence over thermal maturity than burial depth or in-wedge location. This novel inference has probably remained concealed thus far due to the large number of parameters that condition thrust development, frequency, length, and thermal state. Influencing parameters to include sedimentation, erosion, basal friction and relief, pore pressure and fluid state, wedge length and thickness, taper angle, and many others[25,26,47–50]. It is nevertheless important to note that the frequency of faults in a wedge can be impacted by many other factors, including hinterland sedimentation[26,39], erosion[47,51], and seafloor topography[48]. Below, we discuss how thrusts not only alter the thermal evolution of accreting sediments but are, in fact, the primary control on their thermal maturity.

Thermal maturity correlates with sediment depth weakly near faults and more strongly away from them. The distance of sediment from frontal thrust dictates the trajectory of sediment grains, and as a result, the pressure-temperature conditions to which they are exposed. In this study, we have considered solely how décollement strength and the rate of trench sedimentation vary the frequency, architecture, and overall behaviour of thrusts, and the frontal thrust, as the wedge evolves. Our results show the need to consider all factors influencing fault frequency when inferring the geothermal history of contractional terrains by means of thermal maturity. Fortunately, this predictive exercise should be relatively straightforward, for the impact of these external factors on the fault structure of wedges has been established[25,26,39,41,52,53], and the effect of

each of these factors can be accounted for when assessing the trajectory of sediments and the distribution of thermal maturity in accretionary wedges.

Sediment mixing in subduction wedges is primarily controlled by thrusting. Previous studies have reached seemingly contradicting outcomes when using numerical[14,20,24] and analogue[47,54] approaches to analyze sediment trajectories as a function of changes in erosion, sedimentation, or décollement strength. While some studies showed that the rate and extent of a transition by which sediment trajectories change from generally horizontal to increasingly vertical during accretion change consistently with the initial depth of incoming sediments[54,55], others predicted different crossover paths for sediments accreting over a range of décollement strengths[47]. Our models show that both are valid results and that changes in trajectory patterns leading to path crossovers are controlled by the horizontal distance of sediments from the frontal thrust. Starting at a threshold distance from the trench, sediments at different depths follow laminar paths along different trajectories within the wedge. Laminar-type trajectories can be reproduced in a broad range of simulations and are particularly common in models with low sedimentation and décollement strengths. However, the depth dependence of sedimentary paths varies periodically as a function of distance from the trench of specific sedimentary packages (Fig. 2,6). This effect, which is particularly marked in the neighbourhood of the frontal thrust, explains the crossover paths for incoming sedimentary packages at similar depths and different horizontal locations, as shown by Konstantinovskaia et al. 2005. Therefore, thrust faults in the wedge act as the primary agent controlling whether sediments sustain depth-controlled laminar flow or mix.

The thermal maturity that incoming sediments reach varies periodically as a function of thrust frequency. Although previous research considered non-laminar sediment trajectories as chaotic[56], and the wide variety of trajectories shown in our models seem to agree with this (Fig 2), patterns emerge when we correlate the lateral and vertical position of incoming sediments with their eventual thermal maturity. Changes in the depth of the thermal maturity boundary are less frequent and have larger amplitudes with

290 increased décollement strength, and especially, increased sedimentation rates (Fig. 4). The periodicity in
291 the thermal maturity boundary marks the periodic oscillation of the predominant trajectory followed by
292 incoming sediments, i.e., between accretion (low thermal maturity path) and underthrusting (high-thermal
293 maturity path). As a result, it should also strongly correlate with the periodicity observed in the evolution
294 of forearc topography[57]. This is expected, given that thrusts are active over longer mean times, and they
295 thus channel material toward the décollement more efficiently, in wedges with stronger décollement or
296 increased sedimentation. While sediments at internal and higher structural positions of the wedge are
297 translated towards the surface and have a lower thermal maturity, sediments at external and lower structural
298 positions are translated towards the décollement and have a relatively higher maturity. This is a relevant
299 observation, for it typifies the causality of particular sediment grains following a high or low maturity path,
300 a long-standing unanswered question[14]. We corroborate this observation by analyzing the terminal thermal
301 maturity of sediments across a frontal thrust active at a younger age. For example, by showing the thermal
302 maturity of sediments at ~7.5 Myr across a thrust active at ~4 Myr, as in Fig. 7. Whereas this occurs for all
303 thrusts in the wedge, the frontal thrust is particularly pronounced in partitioning sediments into the high and
304 low maturity paths.

305 Geothermal information stored in the incoming sediments can only be retrieved if sediments are at
306 appropriate locations with respect to emergent thrusts. We illustrate this using two runs of the same model
307 and tracking an artificial thermal anomaly imposed on incoming sediments at two different locations (Fig.
308 7). This hypothetical thermal anomaly can be conceptualized as any alteration of the thermal maturity
309 profile of incoming sediments, for example, elevated heat flows by an antecedent magmatic intrusion.
310 While the change in R_0% associated with the short-lived thermal anomaly results in abnormally high values
311 of thermal maturity in both sediment packages, it can only be retrieved for the end-model run of sediments
312 located further from the trench (those in the right panel, Fig. 7b). Contrarily, the end-model run of sediments
313 closer to the trench (those in the left panel, Fig. 7a) shows no signs of discontinuity in the thermal maturity
314 distribution of the wedge. This is because we deliberately placed the thermal anomaly at sites that evolve

315 at two structural locations during the model run, i.e., above and below a yet-undeveloped frontal thrust (Fig.
316 7). The sediment sector affected by the thermal anomaly closer to the trench is overthrusted by the frontal
317 thrust and remains in a footwall location thereafter (Fig. 7a). In contrast, the homologous sedimentary
318 package further away from the trench is accreted by the frontal thrust and remains in a hanging-wall location
319 (Fig. 7b). Thus, the preservation of the record of an antecedent thermal anomaly is only possible in the
320 former case. We further note that, in our simulations, the entire vertical column of sediments records the
321 thermal anomaly, while in nature, the anomaly may affect only sediments at the deeper locations of the
322 sedimentary pile, which are in turn the sediments that most likely to follow a high-maturity path. We thus
323 regard the possibility of retrieving such antecedent geothermal information as minimal.

324 The main implications of this contribution emerge from its predictive power. Our approach can predict to
325 a first-order the thermal maturity of sediments in accretionary contexts with known structuration. More
326 accurate quantification of the thermal evolution and thermal state of accreted sediments reduces the
327 uncertainties attached to the location of temperature-led transformations of organic material into
328 hydrocarbons in subduction margins and other accretionary contexts. Such increased accuracy in the
329 distribution of thermally mature sediments may also be applied for improved assessments of the evolution
330 in time of any other geothermal process, including seismic slip, magmatic and metamorphic extent,
331 porosity, compaction and diagenesis of sediments, and the reconstruction of convergent margins in
332 general[6–9,11,12]

333 # 4. Conclusion

334 This study demonstrates how contractional faults alter the paths of sediments as they accrete and how this
335 fundamentally controls the distribution of the thermal maturity of sediments in accretionary wedges and
336 emphasizes the role that sedimentation rate and interplate contact strength have in such distribution. The
337 increased resolution of our approach leads to findings that have relevant implications. For example, the
338 geothermal history that can be retrieved from the thermal maturity of sediments in drills, i.e., at the shallow

wedge, provides, at best, an incomplete record that is skewed towards the thermal evolution of sediments near the trench. Coevally, relevant sectors of sediments located further seaward, when not subducted, follow high-maturity paths that overprint their antecedent thermal history. Finally, this study also provides a first-order predictive indicator for the thermal maturity of sediments based on the distribution of faults.

References

1. Quigley, T. M. & Mackenzie, A. S. The temperatures of oil and gas formation in the sub-surface. *Nature* **333**, 549–552 (1988).
2. Waples, D. W. *Organic Geochemistry for Exploration Geologists*. (Springer Netherlands, 1981).
3. Tissot, B. P., Pelet, R. & Ungerer, P. H. Thermal History of Sedimentary Basins, Maturation Indices, and Kinetics of Oil and Gas Generation. *AAPG Bull.* **71**, 1445–1466 (1987).
4. Tissot, B. P. & Welte, D. H. *Petroleum Formation and Occurrence*. (Springer Science & Business Media, 2013).
5. Burnham, A. K. & Sweeney, J. J. A chemical kinetic model of vitrinite maturation and reflectance. *Geochim. Cosmochim. Acta* **53**, 2649–2657 (1989).
6. Bostick, N. H. & Pawlewicz, M. J. Paleotemperatures based on vitrinite reflectance of shales and limestone in igneous dike aureoles in the Upper Cretaceous Pierre shale, Walsenburg, Colorado. (1984).
7. Rabinowitz, H. S., Savage, H. M., Polissar, P. J., Rowe, C. D. & Kirkpatrick, J. D. Earthquake slip surfaces identified by biomarker thermal maturity within the 2011 Tohoku-Oki earthquake fault zone. *Nat. Commun.* **11**, 533 (2020).
8. Ferreiro Mählmann, R. & Le Bayon, R. Vitrinite and vitrinite like solid bitumen reflectance in thermal maturity studies: Correlations from diagenesis to incipient metamorphism in different geodynamic settings. *Int. J. Coal Geol.* **157**, 52–73 (2016).
9. Totten, M. W. & Blatt, H. Alterations in the non-clay-mineral fraction of pelitic rocks across the

diagenetic to low-grade metamorphic transition, Ouachita Mountains, Oklahoma and Arkansas. *J. Sediment. Res.* **63**, 899–908 (1993).

10. Schmoker, J. W. & Gautier, D. L. Sandstone porosity as a function of thermal maturity. *Geology* **16**, 1007–1010 (1988).
11. Sakaguchi, A. *et al.* Seismic slip propagation to the updip end of plate boundary subduction interface faults: Vitrinite reflectance geothermometry on Integrated Ocean Drilling Program NanTro SEIZE cores. *Geology* vol. 39 395–398 (2011).
12. Underwood, M. B., Laughland, M. M., Byrne, T., Hibbard, J. P. & DiTullio, L. Thermal evolution of the Tertiary Shimanto Belt, Muroto Peninsula, Shikoku, Japan. *The Island Arc* vol. 1 116–132 (1992).
13. Yamamoto, Y. *et al.* Geothermal structure of the Miura–Boso plate subduction margin, central Japan. *Tectonophysics* **710-711**, 81–87 (2017).
14. Miyakawa, A., Kinoshita, M., Hamada, Y. & Otsubo, M. Thermal maturity structures in an accretionary wedge by a numerical simulation. *Progress in Earth and Planetary Science* **6**, 8 (2019).
15. Platt, J. P. Exhumation of high-pressure rocks: a review of concepts and processes. *Terra Nova* **5**, 119–133 (1993).
16. Ruh, J. B. Numerical modelling of tectonic underplating in accretionary wedges. in 5607 (2020).
17. Giunchi, C. & Ricard, Y. High-pressure/low-temperature metamorphism and the dynamics of an accretionary wedge. *Geophys. J. Int.* **136**, 620–628 (1999).
18. Platt, J. P. Dynamics of orogenic wedges and the uplift of high-pressure metamorphic rocks. *GSA Bulletin* **97**, 1037–1053 (1986).
19. Ruh, J. B. Numerical modeling of tectonic underplating in accretionary wedge systems. *Geosphere* **16**, 1385–1407 (2020).
20. Wenk, L. & Huhn, K. The influence of an embedded viscoelastic–plastic layer on kinematics and mass transport pattern within accretionary wedges. *Tectonophysics* **608**, 653–666 (2013).

21. Hori, T. & Sakaguchi, H. Mechanism of décollement formation in subduction zones. *Geophys. J. Int.* **187**, 1089–1100 (2011).
22. Konstantinovskaia, E. & Malavieille, J. Erosion and exhumation in accretionary orogens: Experimental and geological approaches. *Geochemistry, Geophysics, Geosystems* vol. 6 (2005).
23. Luján, M., Rossetti, F., Storti, F., Ranalli, G. & A. Socquet. Flow trajectories in analogue viscous orogenic wedges: Insights on natural orogens. *Tectonophysics* **484**, 119–126 (2010).
24. Willett, S., Beaumont, C. & Fullsack, P. Mechanical model for the tectonics of doubly vergent compressional orogens. *Geology* vol. 21 371–374 (1993).
25. Mannu, U., Ueda, K., Willett, S. D., Gerya, T. V. & Strasser, M. Impact of sedimentation on evolution of accretionary wedges: Insights from high-resolution thermomechanical modeling. *Tectonics* vol. 35 2828–2846 (2016).
26. Simpson, G. D. H. Formation of accretionary prisms influenced by sediment subduction and supplied by sediments from adjacent continents. *Geology* **38**, 131–134 (2010).
27. Gerya, T. *Introduction to Numerical Geodynamic Modelling*. (Cambridge University Press, 2019).
28. Gerya, T. V. & Yuen, D. A. Characteristics-based marker-in-cell method with conservative finite-differences schemes for modeling geological flows with strongly variable transport properties. *Phys. Earth Planet. Inter.* **140**, 293–318 (2003).
29. Sugihara, T. *et al.* Re-evaluation of temperature at the updip limit of locked portion of Nankai megasplay inferred from IODP Site C0002 temperature observatory. *Earth, Planets and Space* vol. 66 (2014).
30. Crameri, F., Tackley, P. J., Meilick, I., Gerya, T. V. & Kaus, B. J. P. A free plate surface and weak oceanic crust produce single-sided subduction on Earth. *Geophys. Res. Lett.* **39**, (2012).
31. Byrne, T. & Fisher, D. Evidence for a weak and overpressured décollement beneath sediment-dominated accretionary prisms. *Journal of Geophysical Research* vol. 95 9081 (1990).
32. Tobin, H. *et al.* Site C0002. *Proceedings of the IODP* (2015) doi:10.2204/iodp.proc.348.103.2015.

413 33. Fukuchi, R., Yamaguchi, A., Yamamoto, Y. & Ashi, J. Paleothermal structure of the N ankai inner
414 accretionary wedge estimated from vitrinite reflectance of cuttings. *Geochem. Geophys. Geosyst.* **18**,
415 3185–3196 (2017).
416 34. Suzuki, N., Matsubayashi, H. & Waples, D. W. A Simpler Kinetic Model of Vitrinite Reflectance.
417 *AAPG Bull.* **77**, 1502–1508 (1993).
418 35. Tesei, T., Lacroix, B. & Collettini, C. Fault strength in thin-skinned tectonic wedges across the
419 smectite-illite transition: Constraints from friction experiments and critical tapers. *Geology* **43**, 923–
420 926 (2015).
421 36. Korup, O. *et al.* Japan's sediment flux to the Pacific Ocean revisited. *Earth-Sci. Rev.* **135**, 1–16
422 (2014).
423 37. Davis, D., Suppe, J. & Dahlen, F. A. Mechanics of fold-and- thrust belts and accretionary wedges.
424 *Journal of Geophysical Research* vol. 88 1153–1172 (1983).
425 38. Wang, K. & He, J. Mechanics of low-stress forearcs: Nankai and Cascadia. *J. Geophys. Res. [Solid*
426 *Earth]* **104**, 15191–15205 (1999).
427 39. Storti, F. & Mcclay, K. Influence of syntectonic sedimentation on thrust wedges in analogue models.
428 (1995) doi:10.1130/0091-7613(1995)023<0999.
429 40. Malavieille, J. & Trullenque, G. Consequences of continental subduction on forearc basin and
430 accretionary wedge deformation in SE Taiwan: Insights from analogue modeling. *Tectonophysics*
431 **466**, 377–394 (2009).
432 41. Mannu, U., Ueda, K., Willett, S. D., Gerya, T. V. & Strasser, M. Stratigraphic signatures of forearc
433 basin formation mechanisms. *Geochem. Geophys. Geosyst.* **18**, 2388–2410 (2017).
434 42. Dewing, K. & Sanei, H. Analysis of large thermal maturity datasets: Examples from the Canadian
435 Arctic Islands. *Int. J. Coal Geol.* **77**, 436–448 (2009).
436 43. Górszczyk, A., Operto, S., Schenini, L. & Yamada, Y. Crustal-scale depth imaging via joint full-
437 waveform inversion of ocean-bottom seismometer data and pre-stack depth migration of

438 multichannel seismic data: a case study from the eastern Nankai Trough. *Solid Earth* **10**, 765–784
439 (2019).
440 44. Nakanishi, A. *et al.* Three-dimensional plate geometry and P-wave velocity models of the subduction
441 zone in SW Japan: Implications for seismogenesis. *Geology and Tectonics of Subduction Zones: A*
442 *Tribute to Gaku Kimura: Geological Society of America Special Paper* **534**, 69–86 (2018).
443 45. Arai, R. *et al.* Three-dimensional P wave velocity structure of the northern hikurangi margin from
444 the NZ3D experiment: Evidence for fault-bound anisotropy. *J. Geophys. Res. [Solid Earth]* **125**,
445 (2020).
446 46. Ohmori, K. *et al.* Paleothermal structure of the Shimanto accretionary prism, Shikoku, Japan: Role
447 of an out-of-sequence thrust. *Geology* **25**, 327–330 (1997).
448 47. Konstantinovskaia, E. Erosion and exhumation in accretionary orogens: Experimental and geological
449 approaches. *Geochem. Geophys. Geosyst.* (2005).
450 48. Dominguez, S., Malavieille, J. & Lallemand, S. E. Deformation of accretionary wedges in response
451 to seamount subduction: Insights from sandbox experiments. *Tectonics* **19**, 182–196 (2000).
452 49. Ruh, J. B. Effect of fluid pressure distribution on the structural evolution of accretionary wedges.
453 *Terra Nova* **29**, 202–210 (2017).
454 50. Tobin, H. J. & Saffer, D. M. Elevated fluid pressure and extreme mechanical weakness of a plate
455 boundary thrust, Nankai Trough subduction zone. *Geology* **37**, 679–682 (2009).
456 51. Willett, S. D. Orogeny and orography: The effects of erosion on the structure of mountain belts. *J.*
457 *Geophys. Res.* **104**, 28957 (1999).
458 52. Mugnier, J. L. *et al.* Thrust geometry controlled by erosion and sedimentation: A view from
459 analogue models. *Geology* **25**, 427–430 (1997).
460 53. Fillon, C., Huismans, R. S. & van der Beek, P. Syntectonic sedimentation effects on the growth of
461 fold-and-thrust belts. *Geology* **41**, 83–86 (2012).
462 54. Mulugeta, G. & Koyi, H. Episodic accretion and strain partitioning in a model sand wedge.

Tectonophysics **202**, 319–333 (1992).

55. Willett, S. Dynamic and kinematic growth and change of a Coulomb wedge. *McClay, K. R.* 19–31 (1992).

56. Mary, B. C. L., Maillot, B. & Leroy, Y. M. Deterministic chaos in frictional wedges revealed by convergence analysis. *International Journal for Numerical and Analytical Methods in Geomechanics* vol. 37 3036–3051 (2013).

57. Menant, A. *et al.* Transient stripping of subducting slabs controls periodic forearc uplift. *Nat. Commun.* **11**, 1823 (2020).

List of Tables

Table 1: Properties for the different materials used for the model runs

Rock Type	Density (kg/m^3)	Cohesion (MPa)	Coefficient of friction(μ)	Thermal Conductivity (W/(m K))	Flow law	E (kJ/mol)	n
Water	1000	0	0	20		0	0
Air (Sticky-air)	0	0	0	20		0	0
Décollement	2600	0.001	0.03 /0.08	(1.5+807/(T+77))* (1-exp(-Z^2/1.3e7))	Wet quartzite	154	2.3
Sediments1	2600	0.5/0.05*	4.64/0.2*	(0.96+807/(T+77))* (1-exp(-Z^2/1.3e7))	Wet quartzite	154	2.3
Sediments2	2600	0.5/0.05*	4.64/0.2*	(0.96+807/(T+77))* (1-exp(-Z^2/1.3e7))	Wet quartzite	154	2.3
Upper Continental Crust	2700	1	0.6	0.64+807/(T+77)	Wet quartzite	300	2.3
Lower Continental Crust	2800	1	0.6	0.64+807/(T+77)	Wet quartzite	300	3.2
Upper Oceanic Crust	3000	1	0.6	1.18+474/(T+77)	Plagioclase An75	300	2.3
Lower Oceanic Crust	3000	1	0.6	1.18+474/(T+77)	Plagioclase An75	300	3.2
Mantle Lithosphere	3300	1	0.6	0.73+1293/(T+77)	Dry olivine	532	3.5
Asthenosphere	3300	1	0.6	0.73+1293/(T+77)	Dry olivine	532	3.5

**Strain-softened Cohesion/Coefficient of friction*
T is Temperature, Z is the depth from the seafloor.

475 ***Table 2: Model runs and their specific characteristic observations***

Models	φ_b	φ / φ_{ss}	*SR*	*L*	α	*D*	*T*	$\langle R_o\% \rangle$	$\%_{0.75}$	$\%_{0.25}$	*λ(km)*
W_0	**2°**	**30°/15°**	**None**	**74.3±5.7**	**1.2±0.4°**	**4.0±2.2**	**0.20**	**0.39**	**20.9**	**1.2**	**16.1±6.4**
M_0	**7°**	**30°/15°**	**None**	**58.4±5.4**	**4.5±1°**	**3.8±1.6**	**0.25**	**0.49**	**31.9**	**4.1**	**22.6±1.5**
M_1	**7°**	**30°/15°**	**0.1**	**63.4±5.9**	**4.4±1.0°**	**6.4±2.2**	**0.22**	**0.58**	**31.8**	**13.2**	**22.1±3.6**
M_2	**7°**	**30°/15°**	**0.2**	**66.0±7.5**	**3.2±0.8°**	**6.7±2.5**	**0.30**	**0.54**	**46.8**	**12.6**	**24.5±7.8**
M_3	**7°**	**30°/15°**	**0.3**	**70.0±11.4**	**4.0±1.0°**	**9.3±6.4**	**0.44**	**0.66**	**53.0**	**23.5**	**43.2±13.5**
M_4	**7°**	**30°/15°**	**0.4**	**73.0±11.2**	**2.7±1.5°**	**11.1±7.0**	**0.45**	**0.65**	**58.6**	**26.1**	**38.6±11.7**
M_5	**7°**	**30°/15°**	**0.5**	**79.2±15.2**	**2.5±1.4°**	**10.7±10.6**	**0.31**	**0.68**	**62.0**	**33.6**	**50.5±7.6**
M_6	**7°**	**30°/15°**	**0.6**	**83.4±18.7**	**1.1±2.3°**	**12.21±12.2**	**0.34**	**0.70**	**56.4**	**39.7**	**56.7±10.5**
S_0	**12°**	**30°/15°**	**None**	**42.1±4.9**	**18.8±3.1°**	**3.4±2.2**	**0.34**	**0.96**	**69.9**	**36.7**	**50.1±21.6**

φ_b is décollement Strength (internal angle of friction)
φ Sediment Strength
φ_{ss} Sediment Strength (Strain weakened)/(internal angle of friction)
SR Average Sediment rate (mm/yr)
L Average Length between ~3.5-7.5Myr±σ (km)
α Taper angle±σ (in degrees)
D Average Distance between the first and second frontal thrust between ~3.5-7.5Myr
T Average time a frontal thrust remains active between ~3.5-7.5Myr
$\langle R_o\% \rangle$ Average vitrinite reflectance of the wedge between ~3.5-7.5 Myr
$\%_{0.25}$ Proportion of >1.5 eventual ***R_o% (vitrinite reflectance at 7.5 Myr)*** in incoming sediment at 2.5 Myr at a depth of 0.75 km or more from the surface.
$\%_{0.75}$ Proportion of >1.5 eventual ***R_o%*** in incoming sediment at 2.5 Myr at a depth distance of 0.25 km from the surface.
λ Horizontal periodicity of eventual ***R_o%*** in incoming sediment at 2.5 Myr.

List of Figures

Fig. 1: *Distribution of thermal maturity for different models at ~6 Myr. Panels A, B, C, D show the subduction wedges of models W_0, S_0, M_0, and $M_{0.6}$, respectively. Panel E shows the variation of R_0% for an arbitrary horizon of reference shown by the black dashed line. The grey color of the markers indicate that no thermal maturity change in these sediments have occurred.*

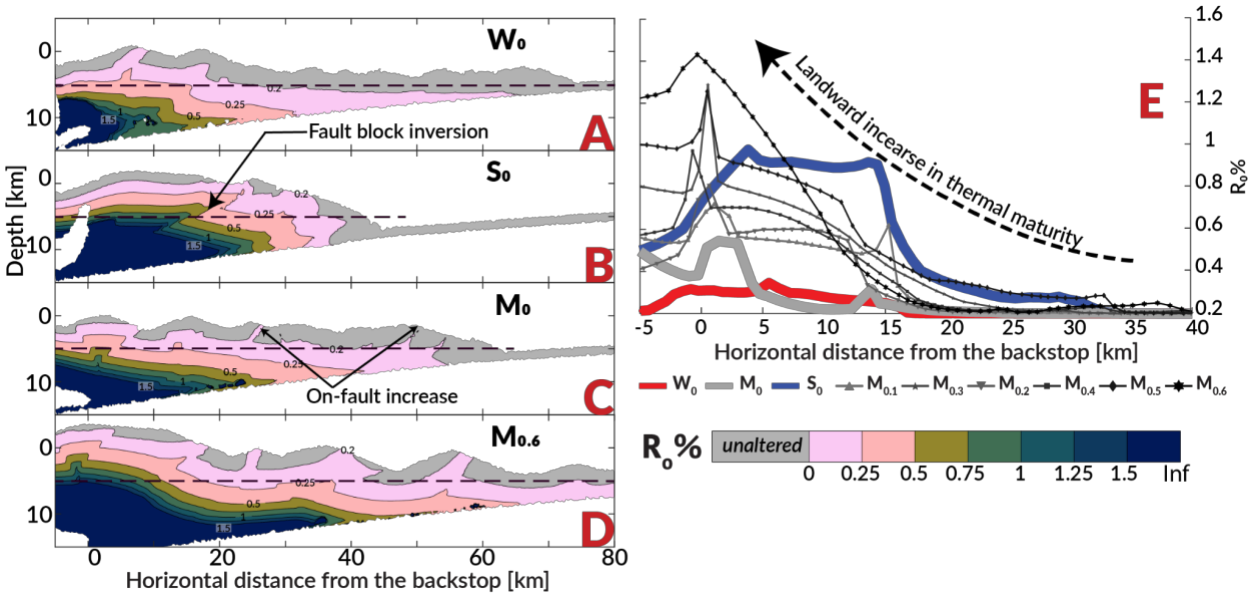

Fig. 2 *Trajectory of sediments in model* W_0 *(weak décollement, no sedimentation, shaded light blue),* S_0 *(strong décollement, no sedimentation, shaded light yellow),* M_0 *(Medium décollement, no sedimentation, shaded light blue),* $M_{0.6}$ *(Medium décollement, high sedimentation, shaded light yellow). The vertical wedge in the left shows the location of individual boreholes relative to the position of the trench at 2.5 Myr. The horizontal wedge on top of each column represents the final wedge geometry at 7.5 Myr. In each borehole, A-L 10 points are plotted for their trajectories between 2.5 Myr and 7.5 Myr. The color of markers in the trajectories represent the evolution of thermal maturity on individual sediment markers while undergoing evolution. The grey color of the markers indicates that no thermal maturity change in these sediments has occurred while the black color indicates they have been eroded during the wedge evolution.*

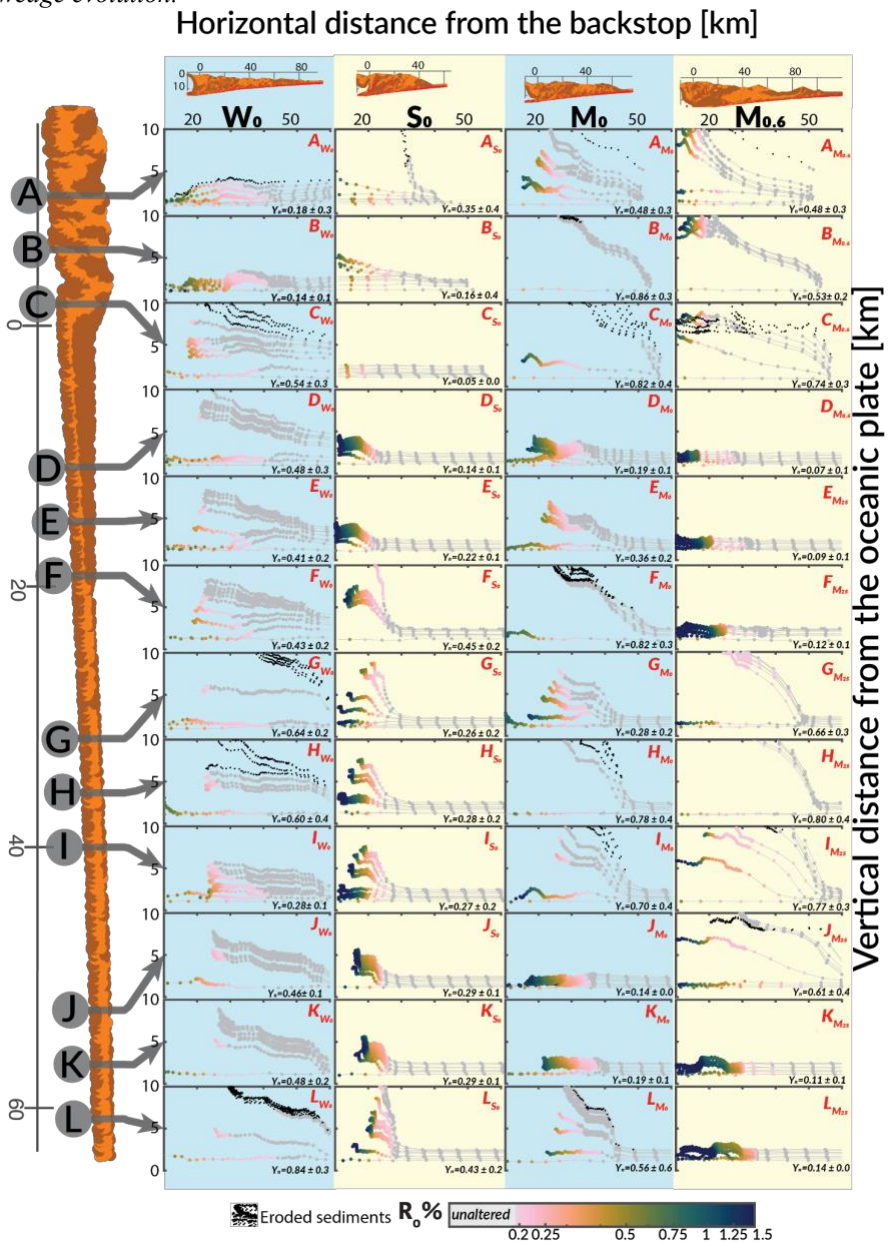

496 ***Fig: 3*** *Vitrinite Reflectance(**R_0%**) vs Average depth of the trajectories normalized by the thickness of the wedge(Y_n)*
497 *for models W_0,S_0 ,M_0 , and $M_{0.6}$ between 2.5-7.5 Myr. Individual points represent trajectory one marker in incoming*
498 *sediment while the patch shows the full spread of R_0%, Y_n values.*
499

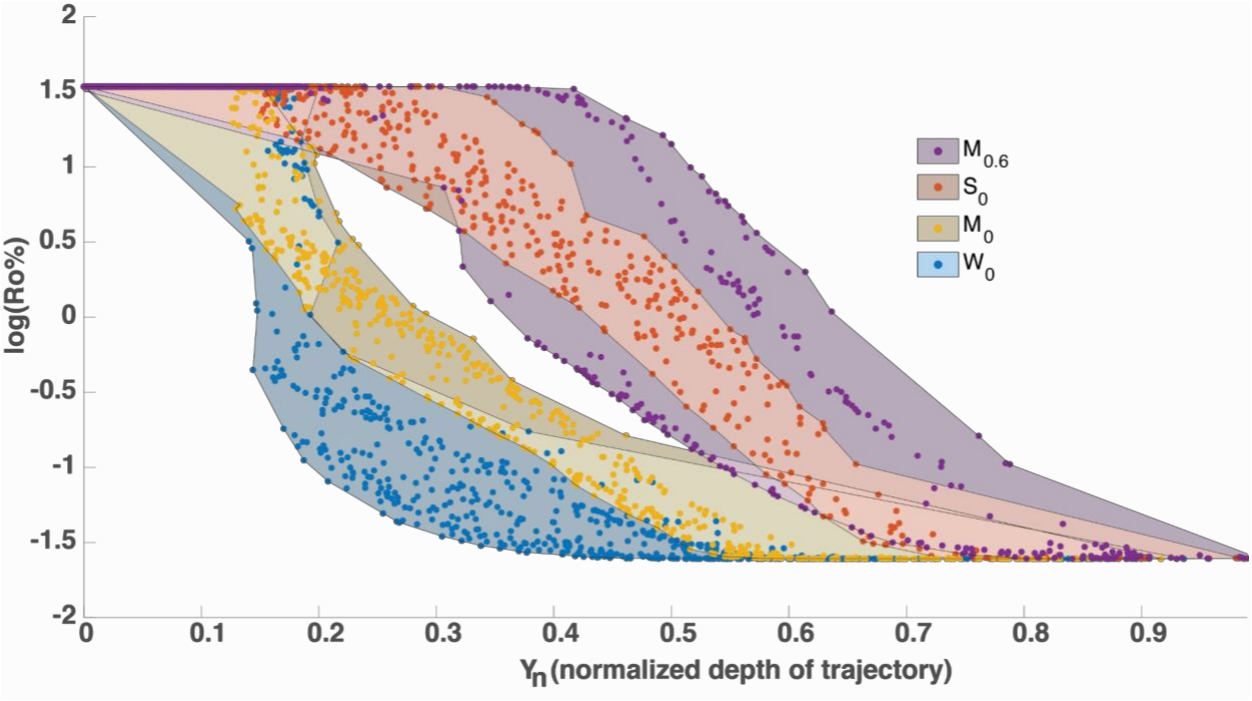

500

Fig. 4: *Contour map of thermal maturity at 7.5 Myr mapped to sediments at 2.5 Myr. Panel A,B,C,D show the mapping for models W_0, S_0, M_0, $M_{0.6}$ respectively. The vertical axis (distance of sediments from the oceanic plate) has been corrected for the bending of the plate(see fig S6 for uncorrected depth). The horizontal axis represents the distance of sediments from the trench. The grey color of the markers indicate that no thermal maturity change in these sediments have occurred. To differentiate between sediments following a high and low maturity path we define an imaginary line $P_{1.5}$ (indicated by the broken yellow line) such that above the line $P_{1.5}$ all sediments take a trajectory such that the final R_0% is less than 1.5.*

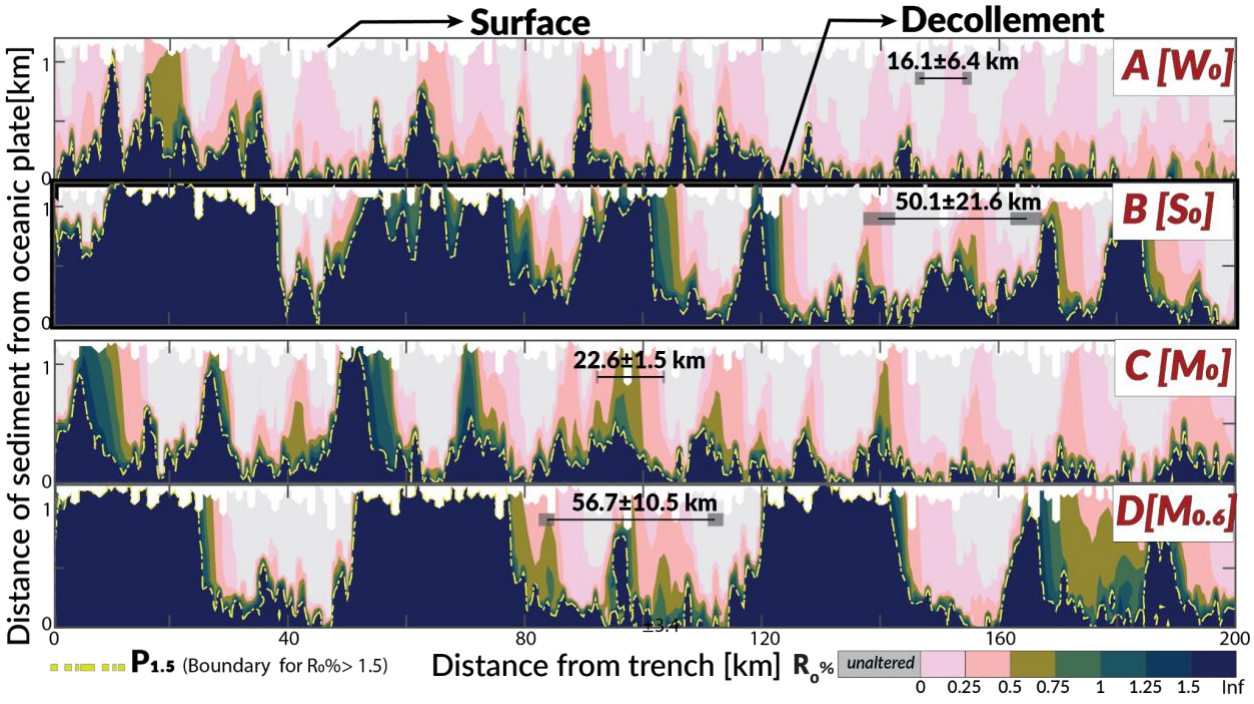

Fig.5: *Depth vs Thermal maturity(R_o%). The shaded (in voilet) region shows the range of observed R_o%(mean±1SD) from the C0002 borehole[33], while the blue dots represent mode of the observation at different depth. The green, red, and black circles, represent the values in models W_0 , M_0 , S_0 . The black and red lines represent the best fitted values for a shifted depth representing an hypothetical erosion.*

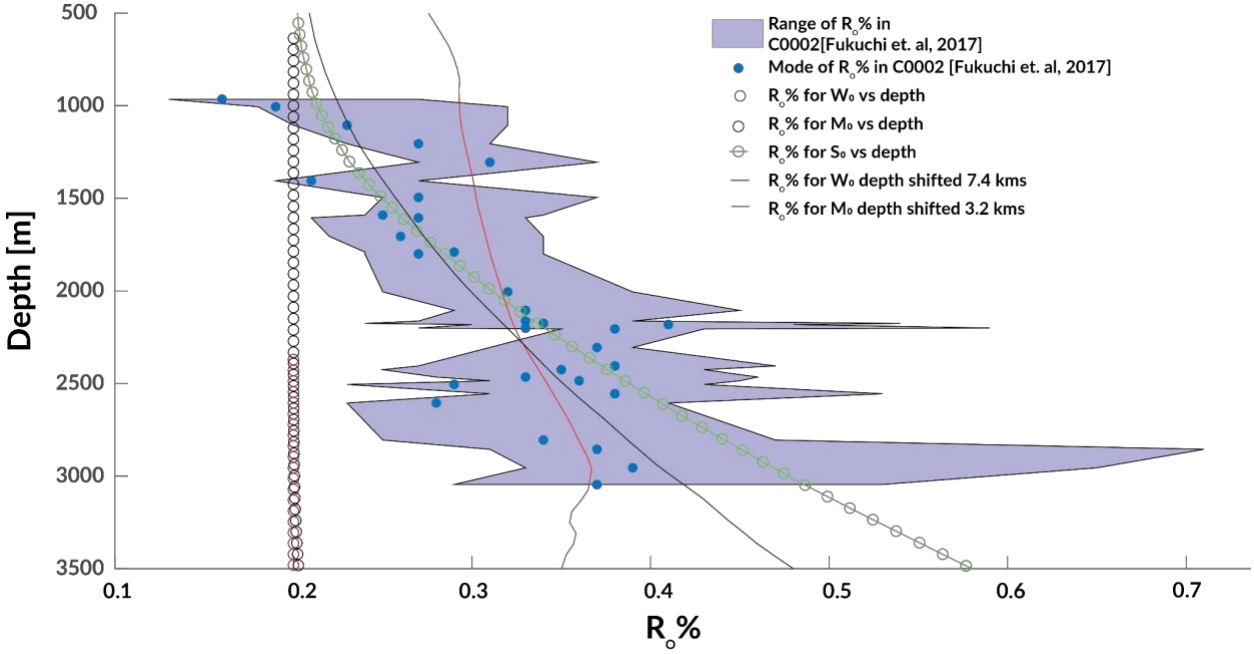

Fig. 6: *Mapping of eventual thermal maturity(vitrinite reflectance at 7.5Myr) to a frontal thrust at ~4Myr in model $M_{0.6}$. A. The lithology of the wedge B. The eventual thermal maturity distribution of the wedge. The half arrow represents the active frontal thrust.*

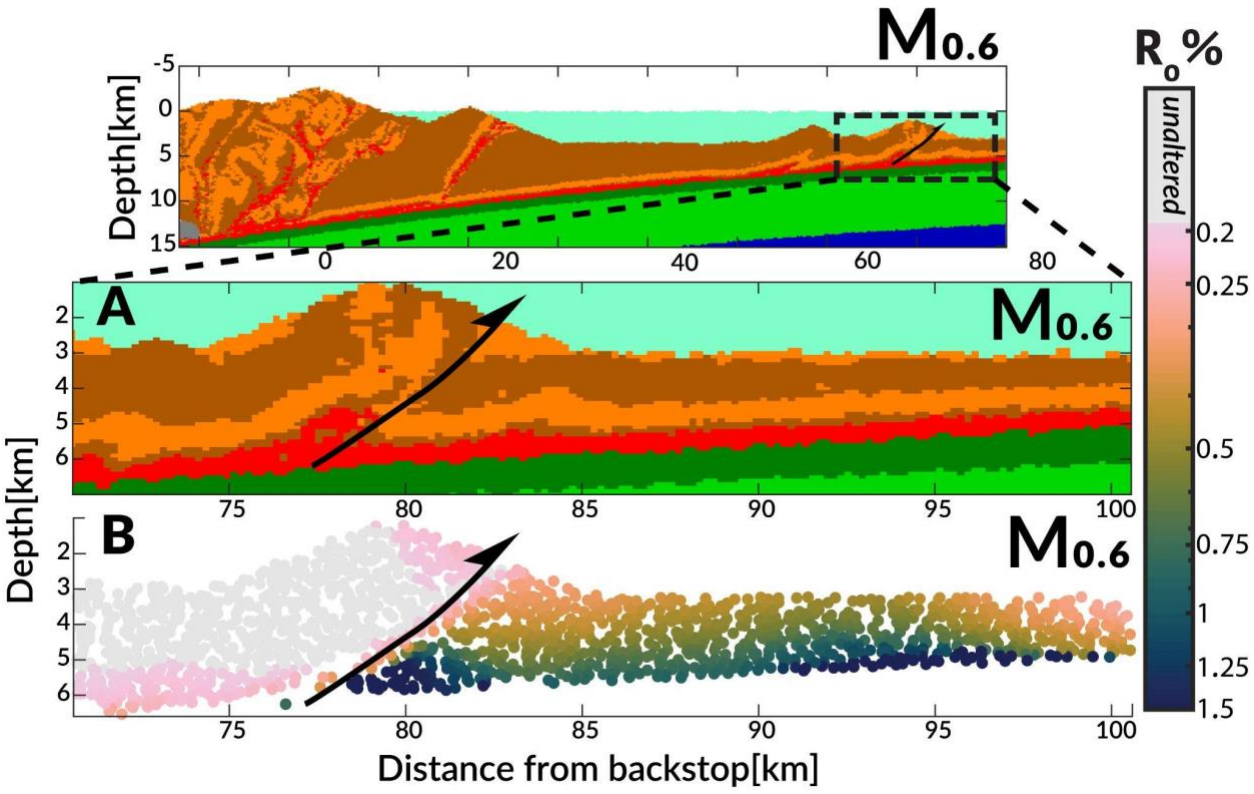

Fig. 7: *Position dependency of thermal maturity preservation. Panel* ***A.*** *Model state at ~2.5 Myr with a thermal anomaly placed at 110-125 km from backstop* ***B.*** *Model state at ~2.5 Myr with a thermal anomaly placed at 140-155 km from the backstop.* ***B.*** *Model state at ~7.5 Myr.*